RSC Advances

PAPER

View Article Online
View Journal | View Issue

Cite this: *RSC Adv.*, 2024, **14**, 35348

Ab initio study of electronic, elastic, thermodynamic, photocatalytic properties of double antiperovskite, Cs_6AgBiX_2 (X = Cl, Br, I)

Laraib Sajid,[a] M. Usman Saeed,[a] S. H. Mashadi,[b] S. Sheryar Abid,[c] Shamiala Pervaiz,[a] Zeeshan Ali,[a] Yousef Mohammed Alanazi,[d] Aziz-Ur-Rahim Bacha [e] and Y. Saeed *[a]

In this paper, we use density functional theory (DFT) using full-potential linearized augmented plan wave plus local orbital method (FP-LAPW + lo). The structural, electronic, optical, photocatalytic, mechanical, vibrational, and thermodynamical behaviors of new double antiperovskite (DAP) Cs_6AgBiX_2 (X = Cl, Br, I) were studied. The band structure was calculated with and without spin orbit coupling (SOC). Using the TB-mBJ approach (Hybrid) revealed bandgap values of 1.504 eV, 1.491 eV, and 1.392 eV for $Cs_6AgBiCl_2$, $Cs_6AgBiBr_2$, and Cs_6AgBiI_2, respectively. Optical characteristics were studied to ascertain the light absorbing ability of Cs_6AgBiX_2. The elastic and vibrational (phonon) properties demonstrate that $Cs_6AgBiCl_2$ and $Cs_6AgBiBr_2$ are stable but Cs_6AgBiI_2 is not. The calculated optimal bandgap and high absorption coefficient of $Cs_6AgBiCl_2$ and $Cs_6AgBiBr_2$, suggest their potential for solar cell applications. Moreover, our photocatalytic results suggest that these materials have high oxidizing capacity that can be used to efficiently produce oxygen cheaply using solar water splitting.

Received 4th August 2024
Accepted 15th October 2024

DOI: 10.1039/d4ra05661b

rsc.li/rsc-advances

1 Introduction

Growing industrialization and fossil fuel use has significantly contaminated the environment and there is now a global energy crisis. To address this, researchers are turning to renewable energy sources, with solar energy being a key focus due to its safety and eco-friendliness.[1–3] Perovskite materials are gaining attention for solar energy use because of their great properties like effective light absorption and improving power conversion efficiency. Researchers have been studying these materials extensively.[4–6]

Perovskite has the crystal structure $CaTiO_3$ and the formula ABX_3, it is used in different forms like antiperovskite X_3BA and double perovskite $A_2B'B''X_6$. These structures offer unique qualities, like easy synthesis and stability.[7–9] A recent addition is the double antiperovskite $X_6B''B'A_2$, showing promise for various applications.[10] Hybrid halide perovskites, like $CH_3NH_3PbX_3$ are widely studied for efficient solar cells but their sensitivity to moisture and use of toxic lead, pose challenges. Seeking stable, lead-free alternatives has led to the exploration of double perovskite halides, such as Cs_2AgBiX_6. These compounds, like $Cs_2AgBiCl_6$ and $Cs_2AgBiBr_6$, are non-toxic and stable, making them promising for solar applications compared to the lead-containing alternatives. The unique structure of halide double perovskites has gained attention as a potential replacement for lead-based perovskite materials.[11–15]

van der Waals (vdW) interactions have been shown to have a significant impact on the geometry optimization and electronic properties of inorganic $CH_3NH_3(Pb,Sn)(I, Br, Cl)_3$ halide perovskites. Studies have focused on the effects of these interactions on the structural and electronic properties of these perovskites. A hydrogen/ionic link between the halogen atoms and an ordinary amine group (NH_3^+) creates the bonding between organic and inorganic components (van der Waals interaction).[16,17] Wang *et al.*[18] presented a PD with a hybrid vdW heterostructure made of graphene (Gr)/1D $CH_3NH_3PbI_3$ and hexagonal boron nitride (h-BN).

However, vdW heterostructures based on double perovskites are still uncommon but are known to have a significant role on the properties of 2D perovskites. Gao *et al.* constructed different heterostructures made up of CsCl, NaInCl, CsNaInCl, and Cl interfaces of the inorganic double perovskite $Cs_2NaInCl_6$ and two-dimensional transition metal–sulfur complexes XS2 (X =

[a]*Department of Physics, Abbottabad University of Science and Technology, Abbottabad, KPK, Pakistan. E-mail: yasir.saeed@kaust.edu.sa; yasirsaeedphy@aust.edu.pk; Tel: +(92)-3454041865*

[b]*Department of Computer Sciences, Abbottabad University of Science and Technology, Abbottabad, KPK, Pakistan*

[c]*Department of Electrical Engineering, University of Azad Jammu & Kashmir, Muzaffarabad, Pakistan*

[d]*College of Engineering, Chemical Engineering Department, King Saud University, Riyadh, Saudi Arabia*

[e]*State Key Laboratory of Urban Water Resource and Environment, Shenzhen Key Laboratory of Organic Pollution Prevention and Control, School of Civil and Environmental Engineering, Harbin Institute of Technology Shenzhen, Shenzhen 518055, P. R. China*

Cr, Mo, and W).[19] Using DFT calculations, properties of the 2D $(C_4H_9NH_3)_2PbI_4$/black phosphorus (BP) vdW heterostructure have been investigated.[20] Furthermore, density functional theory considering vdW, was used to calculate the electron structure and interface properties of inorganic perovskite (without organic cation), results show weak vdW forces between the interfaces of $Cs_2AgBiBr_6$ and $Ti_3C_2T_x$ (to maintain its semiconductor characteristics).[21] There is no study for vdW interactions in 3D inorganic double perovskites or double anti-perovskites as compared to 2D and heterostructures.

Recently, Rani *et al.* explored some new double anti-perovskites Na_6SOCl_2, Na_6SOBr_2, Na_6SOI_2, K_6SOCl_2, K_6SOBr_2 and K_6SOI_2 with bandgaps of 4.34 eV, 3.71 eV, 3.33 eV, 3.99 eV, 3.38 eV and 2.90 eV, respectively, and show that they are good for thermoelectric applications.[22] Yu *et al.* predict that Na_6SOI_2 is specifically appealing for solid sodium-ion battery applications at low temperatures.[23] Mebrouki *et al.* examined the process by which temperature effects the $BaVO_3$ elastic constants C_{11}, C_{12}, and C_{44}, less progressively as temperature rises.[24] Djebari *et al.* calculated the octahedral factor, the formation energy, the tolerance factor *etc.* to confirm the structural stability of $A^{3+}B^{4+}(O_2N)^{7-}$ and $A^{2+}B^{5+}(O_2N)^{7-}$. Based on the computed bandgaps, photovoltaic and ferroelectric devices could find use for them.[25] Gao *et al.* discovered that the coefficient of thermal expansion is negatively impacted by variations in pressure and temperature.[26] Since the double antiperovskite has just recently been proposed, there are not many reports on tests or theoretical calculations, suggesting that this might be a new line of inquiry. Presently, we are examining the features of double antiperovskites Cs_2AgBiX_6 (X = Cl, Br, I). We are examining the expected material's structural, electrical, elastic and optical properties, focusing on those with a bandgap similar to MAPI.[27]

2 Computational details

Using the Wien2k code, we ran our calculations using the full-potential linearized augmented plane wave plus local orbitals (FP-LAPW + lo) technique, which is a component of DFT.[28] Using the more accurate exchange-correlation potential flavor of the generalized gradient approximation (WC-GGA), structural, electrical, and thermodynamic features are investigated.[29] To acquire precise bandgap data, we implemented the modified Becke-Johnson (mBJ) scheme across the WC-GGA.[30,31] In the past, the mBJ plan provided promising band structures and bandgap values for lead halide perovskites and other semiconductors when compared to experimental results.[32–37] The scheme mBJ across WC-GGA gives results close to the experimental results for Cs_6AgBiX_2 (X = Cl, Br and I). The accuracy of our calculations is mainly affected by two factors: one is the total number of k points, so for the Brillouin zone (BZ) integration a k-mesh of $13 \times 13 \times 13$ was used and a finer k-mesh of $24 \times 24 \times 24$ for electronic and optical properties. Another factor is cutoff kinetic energy which determines the number of plane wave expansions inside the muffin-tin radii, here the cutoff energy is set to be −7.0 Ryd, which separates the valence states from the core states of electrons. The plane-wave expansion cutoff was expanded up to $G_{max} = 20$ and the angular momentum of the sphere is $l_{max} = 12$. All structures were optimized with an energy convergence tolerance of up to 10^{-5} Ryd.[38–41]

3 Results and discussion

3.1 Structural properties

Understanding the different physical characteristics of a substance is crucial and understanding structural characteristics is essential for this. Fig. 1 shows the transformation of double perovskite into a double anti-perovskite crystal structure. The proposal aims to optimize the structural properties of Cs_6AgBiX_2 (X = Cl, Br, I) by reducing the energy to its ground state. The starting point for the optimization procedure is the lattice parameter of experimental $Cs_2AgBiCl_6$. The volume optimization curve, which represents the relationship between energy and volume, is plotted in Fig. 2 for Cs_6AgBiX_2 (X = Cl, Br, I). To fit the nonlinear plot of energy *vs.* volume we used the initial lattice parameter values for Cs_2AgBiX_6 (X = Cl and Br) as a reference. The volume optimization was used to calculate structural parameters such as bulk modulus B (GPa) and lattice constant a (Å), for Cs_6AgBiX_2 (X = Cl, Br, I). Table 1 shows the structural characteristics, which were determined by applying

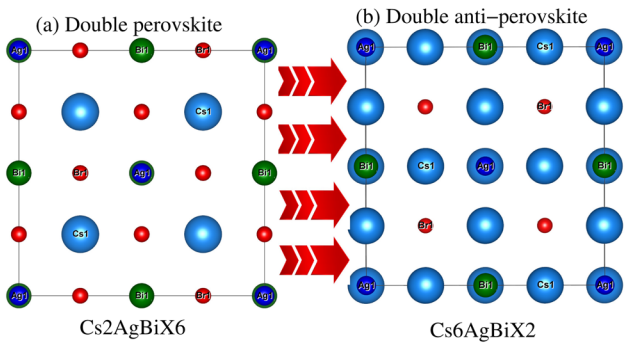

Fig. 1 Prospective view of (a) double perovskite and (b) double anti-perovskite crystal structures.

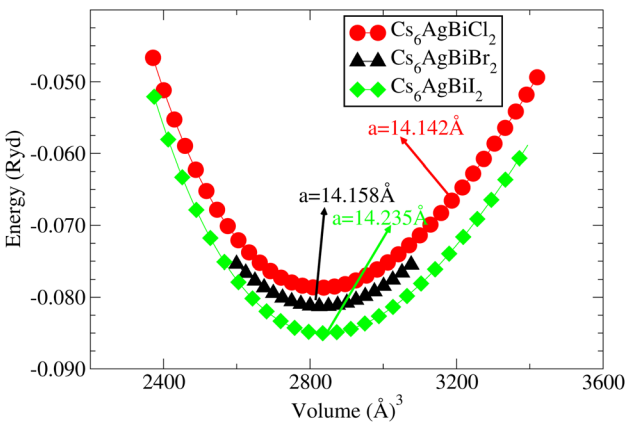

Fig. 2 For cubic double anti-perovskites, the energy *vs.* volume curve, Cs_6AgBiX_2 (X = Cl, Br, I).

Table 1 Optimized lattice parameters, bulk modulus and bandgap of double antiperovskites Cs_6AgBiX_2 (X = Cl, Br, I)

Materials	$a = b = c$ (Å)	Bulk modulus B (GPa)	GGA E_g (eV)	GGA + SOC E_g (eV)	Hybrid E_g (eV)
$Cs_6AgBiCl_2$	14.14	4.63	0.91	0.72	1.50
$Cs_6AgBiBr_2$	14.16	5.10	0.84	0.65	1.49
Cs_6AgBiI_2	14.24	5.16	0.78	0.59	1.39

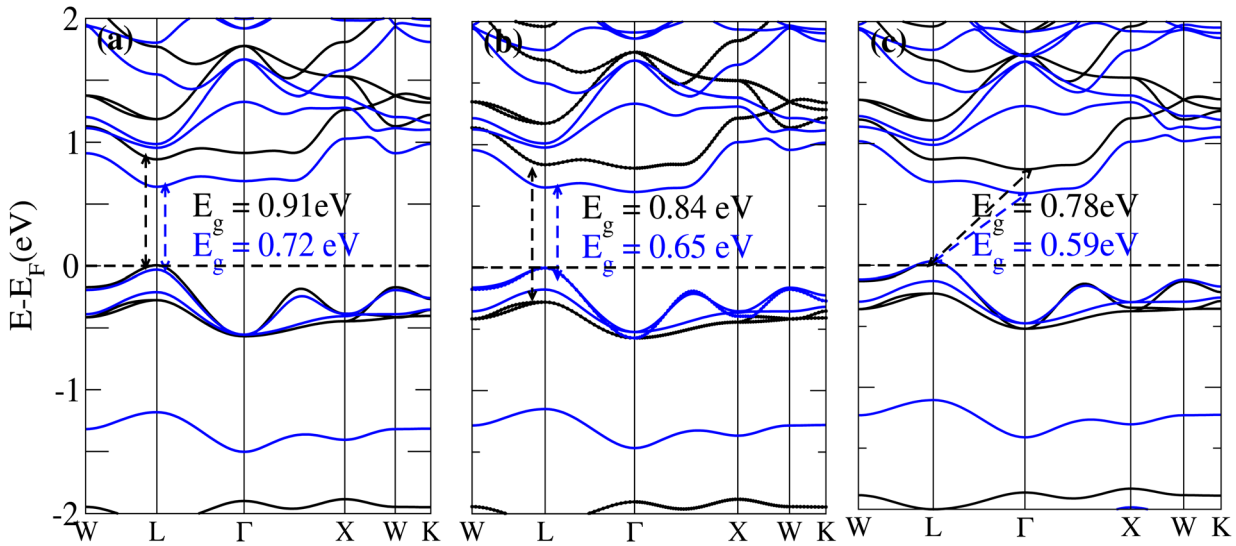

Fig. 3 The band structure of Cs_6AgBiX_2 (X = Cl, Br, I) without SOC (black) and with SOC (blue).

Birch–Murnaghan's equation of states.[44] The optimized lattice constants for all compounds fall within the range 14.14 Å to 14.24 Å, closely aligning with experimentally synthesized double perovskites like $Cs_2AgBiCl_6$ and $Cs_2AgBiBr_6$, which have lattice constants of 10.77 Å and 11.27 Å.[14] The optimized bulk modulus (B) ranges from 4.63 GPa to 5.16 GPa as presented in Table 1. Unfortunately, experimental or theoretical data for comparison with these optimized compounds is not available.

3.2 Electronic band structure

The behavior of a material is profoundly shaped by its band structure, a critical aspect for studying its properties. Analyzing the band structure, including determining its metallic or semiconducting nature, provides valuable insights into the electronic characteristics of the material. This electronic band structure is essential for understanding the optical behaviour and resistivity of solids, which are important for the design of solid-state electronics like solar cells and transistors. The band gap is either direct or indirect, the dispersion of bands informs us of the electronic behavior through which we can specify the physical properties of materials. Consequently, we conducted band structure calculations for Cs_6AgBiX_2 (X = Cl, Br, I) and examined their electronic conduct for further analysis. The initial bandgap calculations for each compound utilized a simple self-consistent field (SCF) approach without considering spin–orbit coupling (SOC). Similarly, this was also done in order to obtain bandgap values that nearly match the experimental bandgap value of MAPI (1.55 eV), producing a straight bandgap as a result at the symmetry point similar to MAPI.[42] Additionally, mBJ + SOC (Hybrid) was utilized to modify the bandgap values in order to better correlate with the experimental MAPI, as a good solar cell absorber. The bandgap of $CH_3NH_3PbCl_3$ is 3 eV, while the band gap of $CH_3NH_3PbBr_3$ is 2.26 eV.[43] The experimental (theoretical) bandgap values for $Cs_2AgBiCl_6$ and $Cs_2AgBiBr_6$, which were previously reported as 2.77 (2.62) eV and 2.19 (2.06) eV, respectively, were recalculated as a baseline with a similar approach.[14,43] We computed bandgap values of 1.50 eV (Cl), 1.49 eV (Br), and 1.39 eV (I) for Cs_6AgBiX_2 (X = Cl, Br, I) with hybrid, respectively. These are close to MAPI, hence proving that anti-double perovskite could reduce the bandgap values substantially as compared to double perovskites. While with SOC, and without SOC, bandgap results are listed in Table 1 and are explained in Fig. 3 and 4.

Our analysis leads to the conclusion that the FP-LAPW + lo technique, without considering mBJ + SOC, tends to substantially underestimate bandgap values in double antiperovskites. Consequently, our objective is to identify a lead-free material with a bandgap value approximately equal to 1.5 eV, serving as a potential replacement for MAPI at room temperature.[45]

The bandgap values for $Cs_6AgBiCl_2$, $Cs_6AgBiBr_2$ and Cs_6AgBiI_2 are 0.91 eV, 0.84 eV and 0.78 eV, in the absence of SOC. The bandgap values of these materials with and without SOC are depicted in Fig. 3a–c. The band structure of $Cs_6AgBiCl_2$ has a bandgap value of 0.91 eV in the absence of SOC and 0.72 eV in

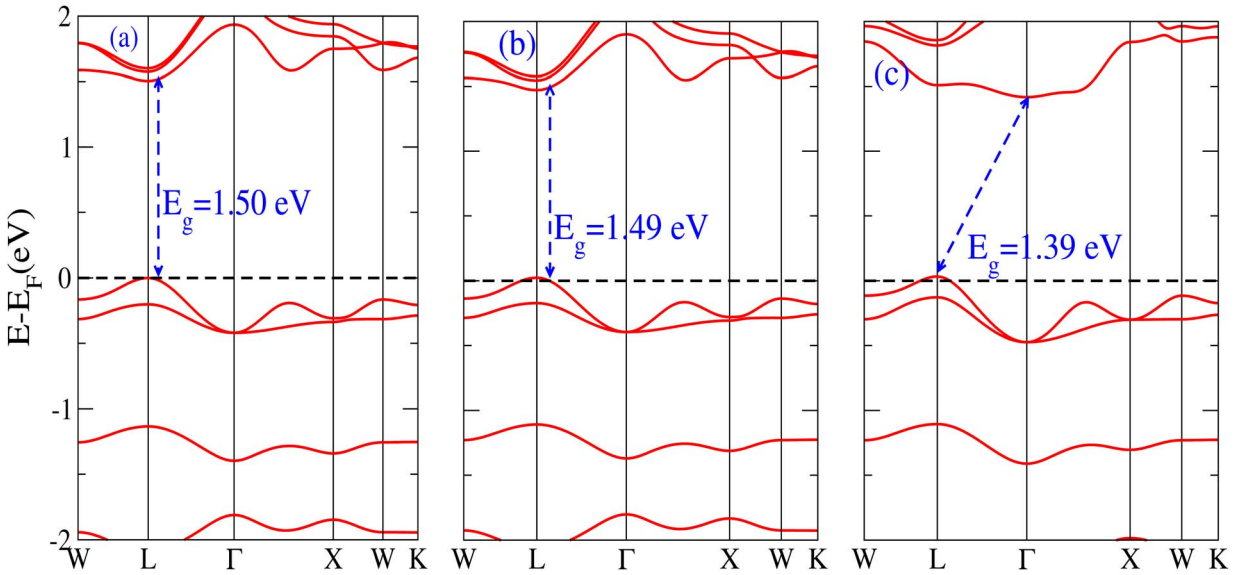

Fig. 4 The band structure of Cs_6AgBiX_2 (X = Cl, Br, I) with hybrid.

the presence of SOC. The band structure of $Cs_6AgBiBr_2$ has a bandgap value of 0.84 eV in the absence of SOC and 0.65 eV in the presence of SOC. These two materials have a direct bandgap as shown in Fig. 3a and b while the band structure of Cs_6AgBiI_2 has a bandgap value of 0.78 eV in the absence of SOC and 0.59 eV in the presence of SOC as shown in Fig. 3c.

It is observed that the bandgap values decreased slightly for Cs_6AgBiX_2 (X = Cl, Br, I) after applying SOC. The bandgap values of $Cs_6AgBiCl_2$ and $Cs_6AgBiBr_2$ align closely with the experimentally calculated values of $CH_3NH_3PbI_3$ (1.55 eV). Within the bandgap of 1.39 to 1.50 eV (see Fig. 4), efficient semiconductor solar cells can be developed, enabling the release of electrons without generating a substantial amount of heat. While some recently investigated double antiperovskites have a direct bandgap, their values exceed this optimal range. Others within the mentioned range, although having an indirect bandgap, are not suitable for solar cell applications. Pressure-induced bandgap tuning could potentially bring the bandgap close to 1.5 eV.

3.3 Density of states (DOS)

We examined the density of states (DOS) for Cs_6AgBiX_2 (X = Cl, Br, I) in order to evaluate the individual contributions of Cs, Ag, Bi, Cl, Br and I atoms to the valence band maxima (VBM) and conduction band minima (CBM), as depicted in Fig. 5a–c.

In Fig. 5a and b, it is evident that the VBM is predominantly influenced by the Cs atom in both materials, while the CBM is shared between Cs and Cl/Br atoms. Notably, Br atoms significantly contribute to the bandgap value. Further insights into the orbital contributions of Cl and Br in the VBM and CBM were gained by examining the PDOS, which is also illustrated in Fig. 5 for Cs_6AgBiX_2 (Cl, Br, I).

The range of the valence band is −3 to 0 and the conduction band range is 0 to 3, and the 0 point represents the Fermi level. Fig. 5a reveals that the Cs-s orbital plays a dominant role in both CBM and VBM, while other atoms have a relatively small contribution compared to these two atoms. The p-orbital of Cl also exhibits significance in the CBM, whereas the contributions of d orbitals are minor in VBM. In VBM, the p-orbital of Bi plays a crucial role, with Cl's p-orbital occupying the entire VBM up to 2 eV, however Br's d-orbital does not contribute much to either the CBM or VBM. Also, compared to Ag and Bi, the effect of Cl's p-orbital on VBM is greater. According to Fig. 5b, comparable patterns are seen in the DOS: Br's p-orbital and Cs's d-orbital completely dominate the CBM and Cs's p-orbital completely dominates the VBM. According to Fig. 5c, similar patterns are seen in the DOS: I's p-orbital and Cs's p-orbital completely dominate the CBM and Cs's d-orbital completely dominates the VBM.

3.4 Optical properties

Studying the optical characteristics of materials is essential from the standpoint of the industrial manufacture of optical devices like sensors, lasers, modulators, solar calculators and optical coatings. One promising option for optical materials production is perovskite high-performing optoelectronic devices.[45,46] The optical characteristics such as the complex dielectric function, $\varepsilon(\omega) = \varepsilon_1(\omega) + i\varepsilon_2(\omega)$, can be utilized to describe a material's reaction to an external electromagnetic field,[47] where $\varepsilon_1(\omega)$ and $\varepsilon_2(\omega)$ are the real and imaginary parts of $\varepsilon(\omega)$. In the relation $\varepsilon_1(\omega)$, is the dielectric constant, which expresses the amount of material polarized by induced electric dipole formation in the presence of an electric field, whereas $\varepsilon_2(\omega)$ indicates the capacity for electromagnetic waves to transmit and attenuate them. The dielectric characteristics $\varepsilon(\omega)$ are closely linked to the combined density of states (DOS) and transition momentum matrix components. The real part of the dielectric function, $\varepsilon_1(\omega)$, can be obtained from $\varepsilon_2(\omega)$ using Kramers–Kronig relationship.[48] The wave is diminishing and cannot propagate if the value of $\varepsilon < 0$; if $\varepsilon_1(\omega) > 0$ light can propagate through the material.[49,50]

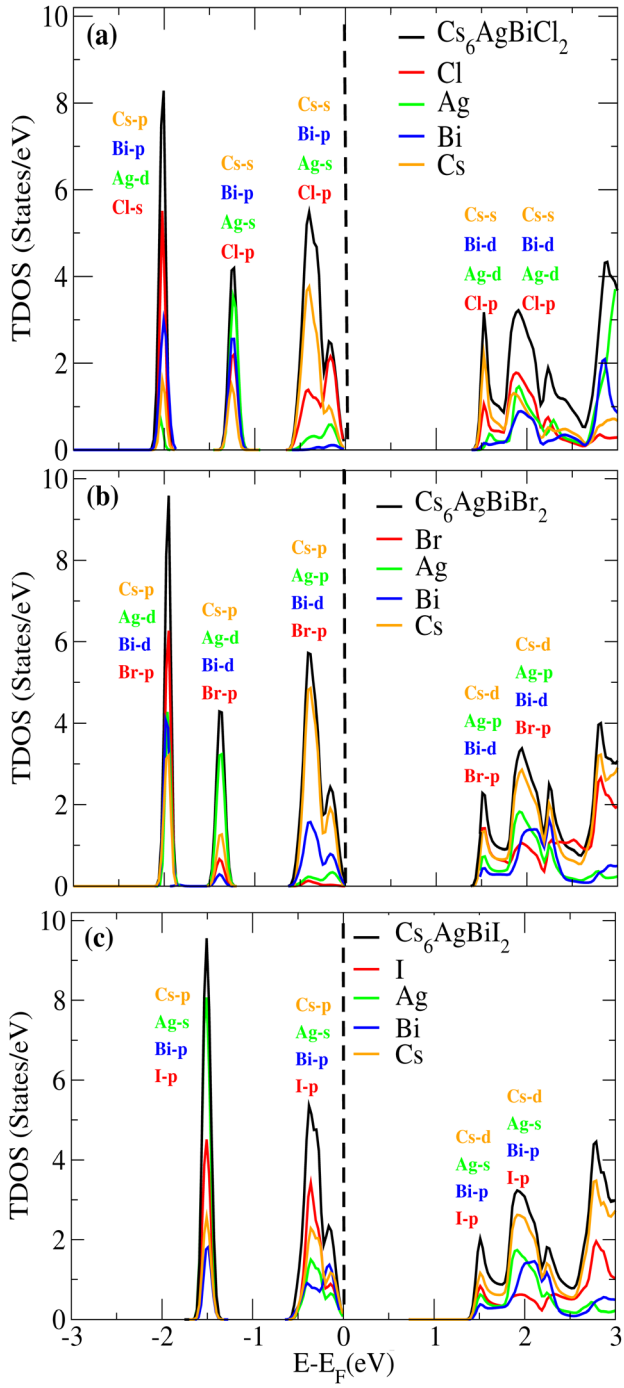

Fig. 5 Density of states (DOS) of (a) $Cs_6AgBiCl_2$, (b) $Cs_6AgBiBr_2$ and (c) Cs_6AgBiI_2.

The dispersion of the real and imaginary components of the dielectric characteristics can be analyzed to compute the refractive index, optical conductivity, reflection and absorption coefficients among other optical properties.

The optical properties of solids can be explained by the refractive index $n(\omega)$ and extinction co-efficients $k(\omega)$. In the case of $n(\omega) < k(\omega)$ the incident rays are reflected and the behavior of materials is dielectric to metallic. It is more advantageous for materials with high dielectric constants to be

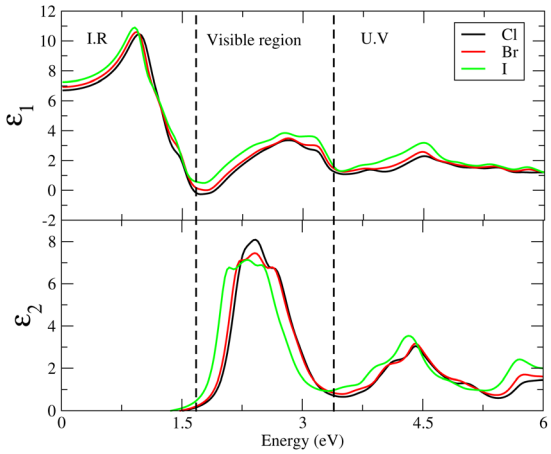

Fig. 6 The dielectric constants for Cs_6AgBiX_2 (X = Cl, Br, I).

used in solar cells since they often have low exciton binding energy.[51]

Cs_6AgBiX_2 (Cl, Br, I) have ε_1 9.57, 9.75 and 10.19, respectively, which are greater than $Cs_2LiTlBr_6$ (1.6), $Cs_2NaTlBr_6$ (1.7), Cs_2AgCrI_6 (5.7), $MAPbI_3$ (5.4) and $FAPbI_3$ (5.7), other potential candidates for solar cell applications.[51–56] It is important to reach maximum polarization characteristics, as indicated by the size of $\varepsilon_1(\omega)$, in order to obtain optimal semiconductor performance. In the visible light range, $\varepsilon_1(\omega)$ approaches peak polarization values of 11.96, 8.77 and 8.63 at 1.0 eV, 0.91 eV, and 0.90 eV, respectively; and $\varepsilon_2(\omega)$ imaginary part shows the light absorption with $\varepsilon_2(\omega)$ values 8.6, 7.9 and 7.5 at −3.0 eV, −3.8 eV, −4.3 eV. None of these compounds are in the visible region. Computations based on the distribution of the dielectric characteristics with real and imaginary parts are shown in Fig. 6, and provide important new information on the linear optical behavior of these materials. We calculated parameters such as the refractive index (n), extinction coefficient (k), absorption coefficient $I(\omega)$, optical conductivity $\sigma(\tau)$, and reflectivity $R(\omega)$, in order to analyze the optical properties of Cs_6AgBiX_2 (X = Cl, Br, I), as illustrated in Fig. 7. For $Cs_2LiTlBr_6$ and $Cs_2NaTlBr_6$, the static dielectric constants $\varepsilon(0)$ are 1.6 eV and 1.7 eV, respectively.[46] So here our study produced comparable findings. Looking at Fig. 7a, we can see that both materials, $Cs_6AgBiCl_2$ and $Cs_6AgBiBr_2$, have a static refractive index ($n(\omega)$) with values of 3.2 and 3.1, respectively. In $Cs_2LiTlBr_6$ the highest values for $n(\omega)$ and $k(\omega)$ are 1.8 eV and 2.6 eV, while for $Cs_2NaTlBr_6$, these values are 2.5 eV for $n(\omega)$ and 3.2 eV for $k(\omega)$. The optical conductivity (σ) of $Cs_6AgBiCl_2$ peaks at 650 $(\Omega\ cm)^{-1}$ at 2.6 eV in Fig. 7b, whereas $Cs_6AgBiBr_2$ peaks at 500 $(\Omega\ cm)^{-1}$ at 3 eV. Because of this, $Cs_6AgBiCl_2$ has exceptionally high optical conductivity in the visible light spectrum (1.77 eV to 3.1 eV) which is important for solar cell applications. The efficiency of solar energy conversion is often described by the absorption coefficient, representing how specific light frequencies penetrate the material before absorption. For $Cs_6AgBiCl_2$ and $Cs_6AgBiBr_2$, the absorption coefficient spectrum $I(\omega)$ shows peaks of $12 \times 10^4\ cm^{-1}$ at 2.6 eV (477 nm) and $11 \times 10^4\ cm^{-1}$ at 3.2 eV, respectively (Fig. 7c). These values are comparable to those of

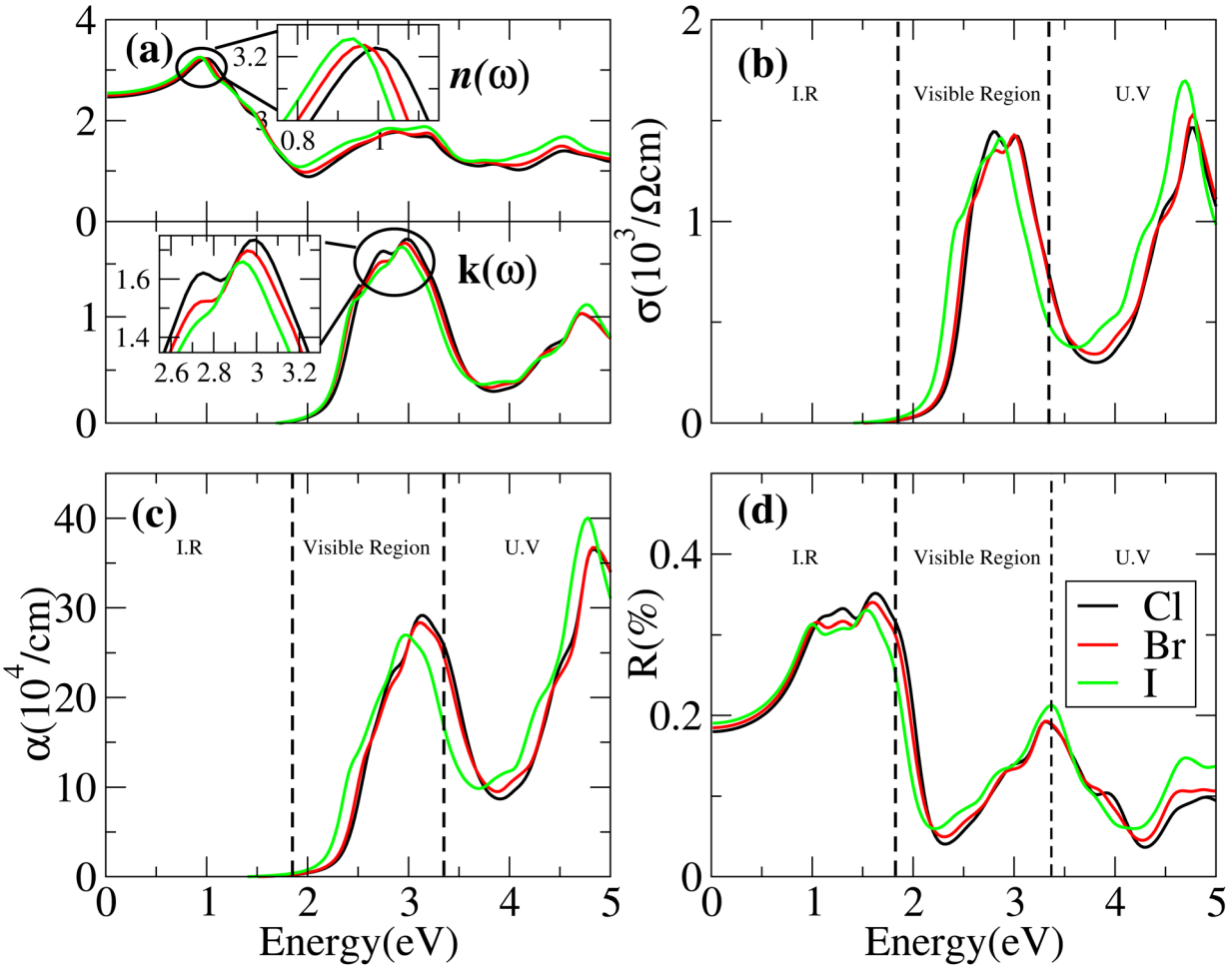

Fig. 7 Optical properties such as (a) refractive index, n and extinction coefficient, k, (b) optical conductivity, σ, (c) absorption coefficient, α, (d) reflectivity, R of $Cs_6AgBiCl_2$, $Cs_6AgBiBr_2$ and Cs_6AgBiI_2.

MAPI (methylammonium lead iodide) at 10^4–10^5 cm^{-1}. The absorption coefficient increases rapidly as incident photons approach the absorption edge, with $Cs_6AgBiCl_2$ exhibiting higher absorption in the visible region compared to $Cs_6AgBiBr_2$. Lastly, in Fig. 7d, the maximum reflectivity $R(\omega)$ for $Cs_6AgBiCl_2$ and $Cs_6AgBiBr_2$ is 13.5% at approximately 1.6 eV and 9% at 2.2 eV, respectively.

3.5 Photocatalytic properties

Suitable indirect bandgap semiconductors can be used to utilize solar energy to generate hydrogen by dissociating water.[57,58] Therefore, clean renewable energy can be produced through photocatalytic water splitting.[59,60] Water is oxidized by holes and reduced by electrons in the photocatalytic process.[61]

Table 2 Photocatalytic parameters of Cs_6AgBiX_2 (X = Cl, Br, I)

Compounds	χ (eV)	E_g (eV)	E_{CBM}	E_{VBM}
$Cs_6AgBiCl_2$	1.17	1.50	−1.06	−2.57
$Cs_6AgBiBr_2$	1.16	1.49	−1.10	−2.59
Cs_6AgBiI_2	1.14	1.39	−1.26	−2.65

The oxidation–reduction potential of O (1.23) eV for this operation needs to be smaller (higher) than the conduction (valence) band photocatalytic water splitting for all materials under consideration (Table 2).

Mullikan electronegativity is used to explore this:

$$E_{VBM} = \chi - E_{elec} + 0.5E_g \quad (1)$$

$$E_{CBM} = E_{VBM} + E_g \quad (2)$$

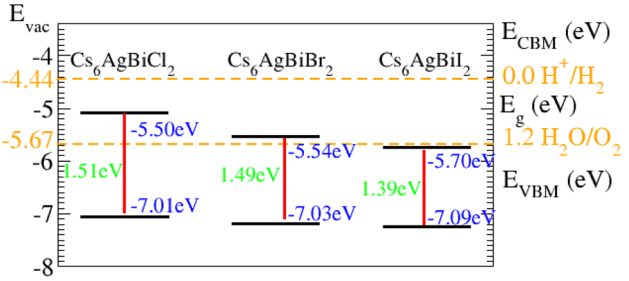

Fig. 8 Photocatalytic properties of $Cs_6AgBiCl_2$, $Cs_6AgBiBr_2$ and Cs_6AgBiI_2.

As displayed in Fig. 8, on the hydrogen scale the standard oxidation and reduction potentials for photocatalytic water splitting are (−4.44 eV) and (−5.67 eV), respectively.[62] The Fermi level is set to (−4.44) eV in order to determine the band edge positions of the VB and CB with respect to standard oxidation.[62] The CB and VB are set to (0 eV = −4.44 eV) and (1.23 eV = ¬5.67 eV).[63] It is clear from the figure that all the materials show good responses for the oxidation of water but fail to produce hydrogen from water.

3.6 Elastic properties

The effective elastic constants are essential for determining a material's practical applications, providing information about its reactivity to outside influences and structural stability. The elastic constants C_{11}, C_{12}, C_{44}, shear moduli G and Bulk moduli B are the key points of elastic properties. These properties help us to understand the material demand in industrial applications. In the case of Cs_6AgBix_2 (x = Cl, Br, I) the calculated elastic constants are detailed in Table 3 and graphical analysis is given in Fig. 9. The materials $Cs_6AgBiCl_2$ are $Cs_6AgBiBr_2$ meet the requirements of Born–Huang stability for cubic crystal stability, that is $C_{11} > 0$, $C_{44} > 0$, $C_{11} + 2C_{12} > 0$, $C_{11} - C_{12} > 0$ and $C_{12} < B < C_{11}$ are satisfied[64] while Cs_6AgBiI_2 does not meet the criteria. So it is unstable.

The elastic constants can be calculated using the following Voigt–Reuss–Hill approximation where, in the formulas $B_V = B_R = C_{11} + 2C_{12}/3$, $G_V = C_{11} - C_{12} + 3C_{44}$ and $G_R = 5C_{44}(C_{11} - C_{12})/(4C_{44} + 3C_{11} - 3C_{12})$, subscripts V and R stand for Voigt bound and Reuss bound, respectively.[65] In Table 3, we can see that the G_v of Cs_6AgBiX_2 (Cl, Br, I) decreases continuously which shows that the resistive behavior of these materials is in the order $Cs_6AgBiCl_2 > Cs_6AgBiBr_2 > Cs_6AgBiI_2$.

Poisson's ratio (ν) or Pugh's ratio (B/G) can be used to evaluate a material's toughness and brittleness. When ν is less than 0.26 or B/G is less than 1.75, the material is considered ductile.[66] Here, only one material, $Cs_6AgBiCl_2$, is ductile while the other two are brittle as their ν and B/G values are greater than 0.26 and 1.75, respectively. Ionic materials typically have a ν range of 0.3–0.4, but the limit for pure ionic materials is 0.5. Covalent materials usually have ν values around 0.2 and for Cs_6AgBiX_2 (X = Cl, Br, I), they are 0.24, 0.28 and 0.59, indicating a greater ionic property than covalent property.[67]

Table 3 Elastic properties of Cs_6AgBiX_2 (X = Cl, Br, I)

Constants	$Cs_6AgBiCl_2$	$Cs_6AgBiBr_2$	Cs_6AgBiI_2
C_{11}	9.5	10.74	9.15
C_{12}	2.22	2.56	3.17
C_{44}	2.38	1.72	−3.65
B	4.64	5.10	5.16
G_v	2.8	2.67	−0.99
G_R	2.7	2.24	−32.67
G_H	2.8	2.45	−16.83
Y	7.17	6.86	−3.18
B/G	1.66	2.15	0.30
C''	−0.16	0.84	6.82
ν	0.24	0.28	0.60
A	0.65	0.42	−1.22
C'	3.64	4.09	2.99
A_z	1.73	1.55	0.54
A_u	0.22	0.95	−4.84
ξ	0.38	0.39	0.49
$T(m)$	609.15	616.48	607.08

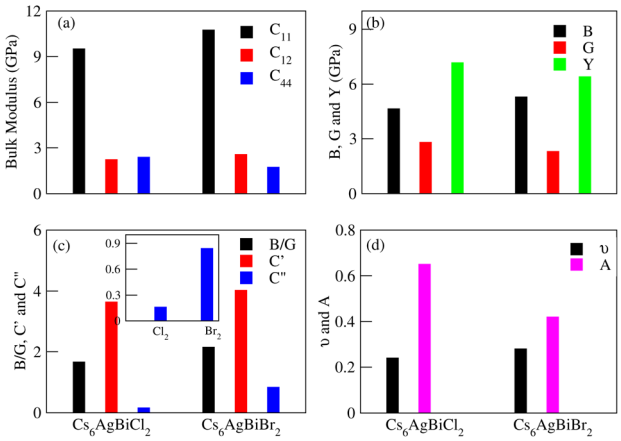

Fig. 9 Graphical view of elastic properties for elastically stable $Cs_6AgBiCl_2$, $Cs_6AgBiBr_2$ and Cs_6AgBiI_2.

Elastic anisotropy is associated with the development of microcracks during the use of a material, we computed this for Cs_6AgBiX_2 (X = Cl, Br, I) using the anisotropy index $A = 2C_{44}/(C_{11} - C_{12})$. A material is isotropic if A is either 0 or 1; otherwise, it exhibits anisotropy.[68,69] The mechanical properties, given in Table 3, were analyzed using standard relations. $Cs_6AgBiCl_2$ shows greater shear modulus (G_H) and Young's modulus (Y) values, indicating greater stiffness and resistance against plastic deformation compared to $Cs_6AgBiBr_2$.

Cauchy's pressure ($C'' = C_{12} - C_{44}$) values, whether positive or negative are presented in Table 3, further elucidate the ductile nature of $Cs_6AgBiCl_2$. The positive values of C'' for $Cs_6AgBiBr_2$ and Cs_6AgBiI_2 reinforce the materials' brittleness. The shear constant (G_H), determining a material's dynamic stability, has a positive value for $Cs_6AgBiCl_2$, $Cs_6AgBiBr_2$ and Cs_6AgBiI_2 in Table 3, affirming their mechanical stability.

In order to graphically portray the anisotropic and elastic behavior of the materials under study, three-dimensional (3-D) contour plots of the Young's modulus (Y), linear compressibility (β), shear modulus (G), and Poisson's ratio (ν) have been created using the Elate Code.[70] Fig. 10 and 11, respectively, show the resulting 3-D visual representations for $Cs_6AgBiCl_2$ and $Cs_6AgBiBr_2$. Notably, all other constants show large deviations from a fully spherical (3-D) shape, with the exception of linear compressibility, highlighting the anisotropic character of these materials.

Additionally, anisotropic parameters, such as Zener (A_Z) and Universal anisotropic parameters (A_U), have been determined using the second-order elastic constants (SOECs).[71,72] Table 3 presents the computed values for these parameters. In isotropic materials, the Zener elastic parameter, which is mainly related to shear anisotropy in materials, stays constant at 1. But any departure from unity, as we can observe in A_U and A_Z in Table 3, indicates that the material under study exhibits anisotropic

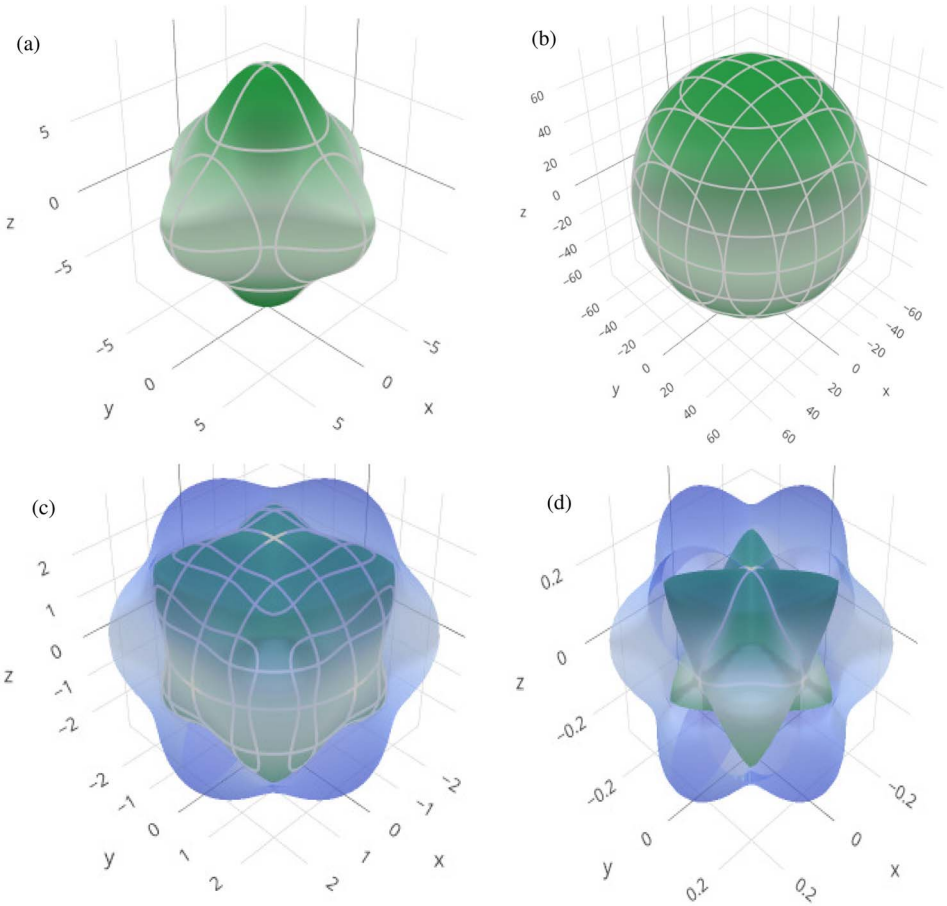

Fig. 10 3D spatial dependence of (a) Young's modulus, (b) linear compressibility, (c) shear modulus and (d) Poisson's ratio for $Cs_6AgBiCl_2$.

behavior. The elastic constants have later been used to calculate the Kleiman parameter (ξ). Table 3 indicates that the materials have a higher resistance against bond angle distortions and bond bending due to the observed low value of ξ.

We determined the melting temperature using the following equation in order to assess their stability at high temperatures,[73]

$$T(m) = [553 + 5.911C_{11}] \pm 300 \quad (3)$$

The predicted melting temperatures are determined to be 609.15 ± 300 K for $Cs_6AgBiCl_2$, 616.48 ± 300 K for $Cs_6AgBiBr_2$ and 607.08 ± 300 K for Cs_6AgBiI_2. Notably, the high value of the melting temperature suggests that these materials exhibit stability even under extreme temperatures.

3.7 Phonon dispersion and thermal properties

To further confirm the stability, adding to the elastic constant results, we use a 2 × 2 × 2 supercell in the well -established PHONOPY package.[74,75] The calculated phonon band structures of $Cs_6AgBiCl_2$, $Cs_6AgBiBr_2$ and Cs_6AgBiI_2 are shown in Fig. 12a–c. $Cs_6AgBiCl_2$ and $Cs_6AgBiBr_2$ are dynamically stable which also validates the elastic results, while Cs_6AgBiI_2 has negative phonon frequencies up to $-25\ cm^{-1}$. Hence, Cs_6AgBiI_2 has been shown to be unstable by elastic as well as vibrational analysis.

Aside from these elastic constants, Debye temperature (Θ_D) is an important thermal parameter that is closely linked to several physical properties such as a compound's melting point and specific heat capacity. It is possible to calculate Debye temperature using average sound velocity v_m.[76]

$$\Theta_D = \frac{h}{k}\left[\left(\frac{3n}{4\pi}\right)\left(\frac{N_A\rho}{M}\right)\right]^{\frac{1}{3}} v_m \quad (4)$$

The variables h, k, n, N_A, ρ, and M stand for Planck's constant, Boltzmann constant, atomic number, Avogadro's number, material density, and molecular mass, respectively. The stronger the connection, the higher the Debye temperature or sound velocity. The average sound velocity in polycrystalline materials can be expressed as follows:[77]

$$v_m = \left[\frac{1}{3}\left(\frac{2}{v_t^3} + \frac{1}{v_l^3}\right)\right]^{-\frac{1}{3}} \quad (5)$$

where v_t and v_l are the transverse and longitudinal sound velocities, respectively, that may be derived using Navier's equation and elastic constants (B and G).[78]

$$v_t = \sqrt{\frac{G}{\rho}} \quad (6)$$

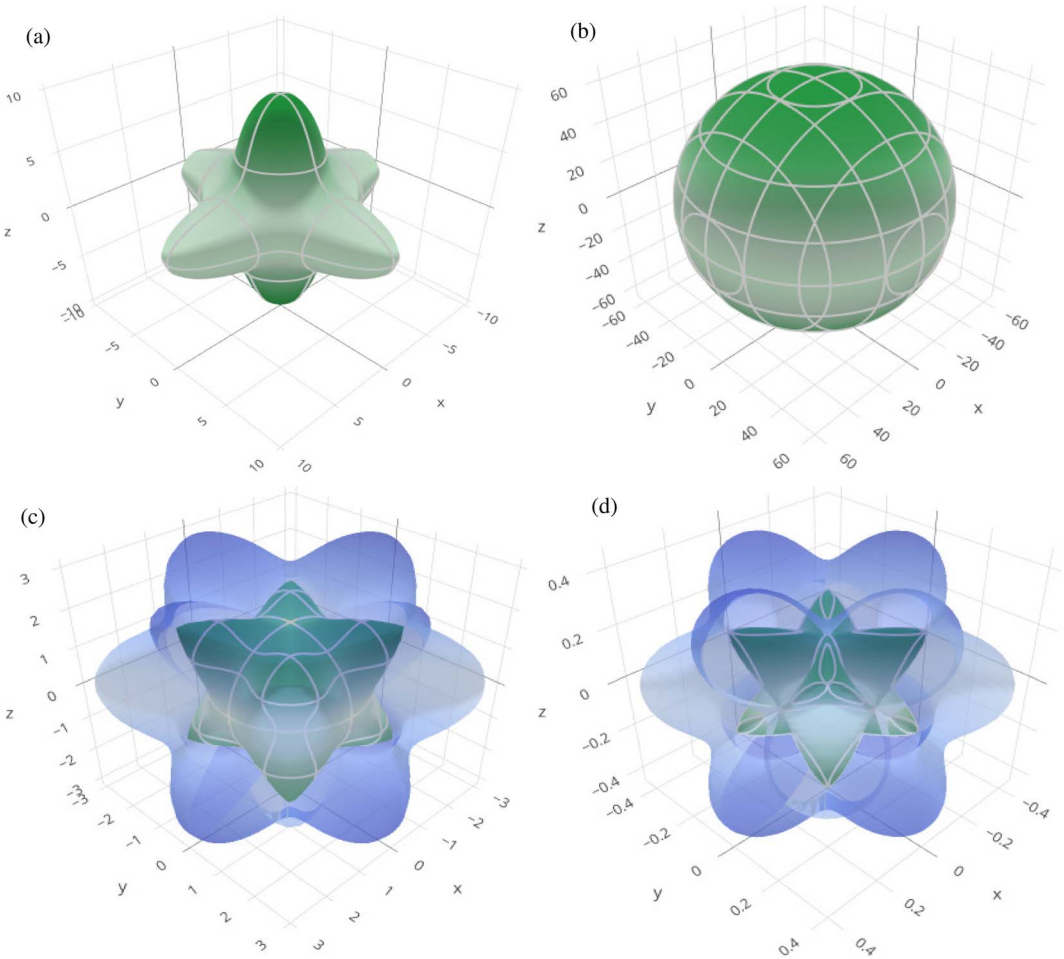

Fig. 11 3D spatial dependence of (a) Young's modulus, (b) linear compressibility, (c) shear modulus and (d) Poisson's ratio for $Cs_6AgBiBr_2$.

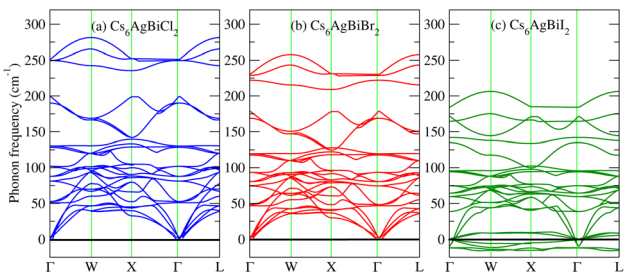

Fig. 12 Calculated phonon band structures of Cs_6AgBiX_2 (X = Cl, Br, I).

Table 4 Thermal properties of $Cs_6AgBiCl_2$ and $Cs_6AgBiBr_2$

Compound	$Cs_6AgBiCl_2$	$Cs_6AgBiBr_2$
v_t (m s^{-1})	1006.9	904.04
v_l (m s^{-1})	1737.84	1670.64
v_m (m s^{-1})	1086.32	985.35
Θ_D (K)	473.6	451.3
ω_D (THz)	61.9	58.9

$$v_l = \sqrt{\frac{3B + 4G}{3\rho}} \quad (7)$$

Table 4 displays the values of v_t, v_l, v_m, and Θ_D that were derived from the aforementioned relations. $Cs_6AgBiCl_2$ and $Cs_6AgBiBr_2$ have the highest Debye temperature indicating that these are thermally more conductive. These findings also provide insight into the bond strength hierarchy.

4 Conclusion

In this work, structural, electronic, optical, photocatalytic, mechanical, vibrational, and thermodynamical behaviors were studied for new double antiperovskite (DAP) Cs_6AgBiX_2 (X = Cl, Br, I). Band structures were calculated with and without spin orbit coupling (SOC). Using the TB-mBJ approach (hybrid) reveals bandgap values of 1.504 eV, 1.491 eV, and 1.392 eV for $Cs_6AgBiCl_2$, $Cs_6AgBiBr_2$, and Cs_6AgBiI_2 respectively. To gain deeper insight into the orbital contributions of chlorine (Cl),

bromine (Br), and iodine (I) near the Fermi level, analysis of the total density of states (TDOS) and partial density of states (PDOS) were studied. In addition to electronic properties, the investigation extended to optical properties, including real and fictitious refractive indexes, extinction coefficients, optical conductivities, absorption coefficient, and reflectivity. The elastic and phonon properties demonstrate that $Cs_6AgBiCl_2$ and $Cs_6AgBiBr_2$ are stable except Cs_6AgBiI_2. The calculated optimal bandgap (~1.5 eV) and high absorption coefficient (~30×10^4 cm^{-1}) of $Cs_6AgBiCl_2$ and $Cs_6AgBiBr_2$, suggest their potential for solar cell applications. In addition, our photocatalytic results suggest that these Cs_6AgBiX_2 have more oxidizing capacity due to good visible-light absorption capability that can be used for cheap oxygen production *via* solar water splitting.

Data availability

Data will be made available upon request.

Conflicts of interest

The authors declare that they have no known competing financial interests or personal relationships that could have appeared to influence the work reported in this paper.

Acknowledgements

The authors would like to acknowledge the Researcher's Supporting Project Number (RSP2024R511), King Saud University, Riyadh, Saudi Arabia. The author Y. Saeed would like to thank the Higher Education Commission (HEC) of Pakistan for providing a grant under NRPU-15844.

References

1 T. Wu, M. L. Yao and M. Q. Long, First principle calculations of interface interactions and photoelectric properties of perovskite $CsPbX_3$ (X = Cl, Br, I) and penta-graphene van der Waals heterostructures, *Acta Phys. Sin.*, 2021, **70**, 056301.

2 H. K. Ting, L. Ni, S. B. Ma, Y. Z. Ma, L. X. Xiao and Z. J. Chen, Progress in electron-transport materials in application of perovskite solar cells, *Acta Phys. Sin.*, 2015, **64**, 038802.

3 P. Zhao, J. Su, Y. J. Guo, Z. H. Wang, Y. Lin, X. P. Hao, Ouyang and J. J. Chang, Cs_2TiI_6: a potential lead−free all−inorganic perovskite material for ultrahigh−performance photovoltaic cells and alpha-particle detection, *Nano Res.*, 2022, **15**, 2697–2705.

4 Y. Guo, Y. B. Xue and L. Q. Xu, Interfacial interactions and enhanced optoelectronic properties of GaN/perovskite heterostructures: insight from first-principles calculations", *J. Mater. Sci.*, 2021, **56**, 11352–11363.

5 G. M. Sui, G. J. Yan, G. Yang, B. Zhang and Y. Q. Feng, Theoretical investigation on structure and optoelectronic performance of two-dimensional fluorbenzidine perovskites, *Acta Phys. Sin.*, 2022, **71**, 208801.

6 D. Wang, H. M. Zhu, Z. M. Zhou, Z. W. Wang, S. L. Lv, S. P. Pang and G. L. Cui, Effect of solvent on the perovskite thin film morphology and crystallinity, *Acta Phys. Sin.*, 2015, **64**, 038403.

7 Y. B. Fu, H. Wei, L. Wei, H. D. Zhang, X. P. Wang, B. Liu, Y. Y. Zhang, X. S. Lv, J. X. Zhou and H. J. Yu, Origin of the difference in thermal conductivity and anharmonic phonon scattering between $LiNbO_3$ and $LiTaO_3$, *CrystEngComm*, 2021, **23**, 8572–8578.

8 Y. N. Xiao, P. F. Sui, Y. C. Zhao, J. Ni, S. Meng and Z. H. Dai, Low lattice thermal conductivity of hydride-based cubic antiperovskites A3HB (A = Li, Na; B = S, Se, Te) with higher−order anharmonicity correction, *Int. J. Energy Res.*, 2022, **46**, 13687–13697.

9 Y. Liu, L. H. Ni, G. Xu, C. L. Song, G. R. Han and Y. Zheng, Phase transition in PbTiO3 under pressure studied by the first−principles method, *Phys. B*, 2008, **403**, 3863–3866.

10 D. Han, C. B. Feng, M. H. Du, T. Zhang, S. Z. Wang, G. Tang, T. Bein and H. Ebert, Design of high−performance lead−free quaternary antiperovskites for photovoltaics via ion type inversion and anion ordering, *J. Am. Chem. Soc.*, 2021, **143**, 12369–12379.

11 J. Chen, X. Cai, D. Yang, D. Song, J. Wang, J. Jiang, A. Ma, S. Lv, M. Z. Hu and C. Ni, Recent progress in stabilizing hybrid perovskites for solar cell applications, *J. Power Sources*, 2017, **355**, 98–133.

12 M. J. Fang, C. W. Tsao and Y. J. Hsu, Semiconductor nanoheterostructures for photoconversion applications, *J. Phys. D: Appl. Phys.*, 2020, **53**, 143001–143026.

13 Y. H. Chiu, T. H. Lai, M. Y. Kuo, P. Y. Hsieh and Y. J. Hsu, Photoelectrochemical cells for solar hydrogen production: Challenges and opportunities, *APL Mater.*, 2019, **7**, 080901–080911.

14 Y. Saeed, B. Amin, H. Khalil, F. Rehman, H. Ali, M. I. Khan, A. Mahmood and M. Shafiq, Correction: Cs2NaGaBr6: a new lead-free and direct bandgap halide double perovskite, *RSC Adv.*, 2020, **10**, 17444–17451.

15 M. Z. Rehman, S. A. M. Abdelmohsen, E. A. Mahmoud, M. U. Saeed, M. Idress, M. Shafiq, B. Amin and Y. Saeed, First principles study of structural, electronic, elastic and optical properties of $Cs_2LiTlBr_6$ and $Cs_2NaTlBr_6$, *Mater. Sci. Semicond. Process.*, 2022, **151**, 106993.

16 N. Pandech, T. Kongnok, N. Palakawong, S. Limpijumnong, W. R. Lambrecht and S. Jungthawan, Effects of the van der Waals Interactions on Structural and Electronic Properties of CH_3NH_3(Pb, Sn)(I, Br, Cl)$_3$ Halide Perovskites, *ACS Omega*, 2020, **5**, 25723–25732.

17 H. Ferjani, Y. B. Smida and Y. Al-Douri, First-Principles Calculations to Investigate the Effect of Van der Waals Interactions on the Crystal and Electronic Structures of Tin-Based 0D Hybrid Perovskites, *Inorganics*, 2022, **10**, 155.

18 G. Wang, B. Han, C. H. Mak, J. Liu, B. Liu, P. Liu, X. Hao, H. Wang, S. Ma, B. Xu and H.-Y. Hsu, Mixed-dimensional van der waals heterostructure for high-performance and air-stable perovskite nanowire photodetectors, *ACS Appl. Mater. Interfaces*, 2022, **14**, 55183–55191.

19 S. Gao, W. Chen, E. Abduryim, C. Chen, C. Dong, Y. Kuai, X. Guan and P. Lu, Double-perovskite van der Waals heterostructure Cs2NaInCl6-XS2 (X=Cr, Mo, W) as great

potential material in photovoltaic devices, *Surf. Interfaces*, 2023, **37**, 102734.

20 D. Li, D. Li, A. Yang, H. Zhang, X. Lai and C. Liang, Electronic and Optical Properties of van der Waals Heterostructures Based on Two-Dimensional Perovskite $(PEA)_2PbI_4$ and Black Phosphorus, *ACS Omega*, 2021, **6**, 20877–20886.

21 L. Yang, P. Hou, B. Wang, C. Dall'Agnese, Y. Dall'Agnese, G. Chen, Y. Gogotsi, X. Meng and X.-F. Wang, Performance improvement of dye-sensitized double perovskite solar cells by adding $Ti_3C_2T_x$ MXene, *Chem. Eng. J.*, 2022, **446**, 136963.

22 U. Rani, P. K. Kamlesh, R. Agarwal, J. Kumari and A. S. Verma, Electronic and thermo-physical properties of double antiperovskites X_6SOA_2 (X = Na, K and A = Cl, Br, I): a non−toxic and efficient energy storage materials, *Int. J. Quantum Chem.*, 2021, **121**, 26759.

23 Y. Yu, Z. Wang and G. S. Shao, Theoretical design of double anti-perovskite Na_6SOI_2 as a super−fast ion conductor for solid Na^+ ion batteries, *J. Mater. Chem. A*, 2018, **6**, 19843–19852.

24 M. Mebrouki, T. Ouahrani and Y. O. Ciftci, Unraveling thermal and dynamical properties of the cubic $BaVO_3$ perovskite from first−principles calculation, *Int. J. Thermophys.*, 2016, **37**, 71–80.

25 K. Djebari, A. Dahani, M. Djermouni, K. Dine, A. Cherif, O. Arbouche, A. Zaoui and S. Kacimi, Spontaneous polarization study in $A^{3+}B^{4+}(O_2N)^{7-}$ and $A^{2+}B^{5+}(O_2N)^{7-}$ perovskite-type oxynitrides: a first principles investigation", *Appl. Phys. A: Mater. Sci. Process.*, 2022, **128**, 398–410.

26 Q. Gao, R. Y. Ma, L. Li, H. H. Xie, J. B. Deng and X. R. Hu, First-principle study on compensated half metallic double perovskite compound Ba_2PrVO_6, *J. Supercond. Novel Magn.*, 2017, **30**, 545–554.

27 H. X. Gao, De-Y. Hu, T.-Yu Tang, Qi-Qi Liang, Qi Dai, S.-S. Wu and Y.-L. Tang, First-principles study on the structural, electronic, elastic, optical and thermodynamic properties of double antiperovskites X_6BiSbN_2 (X = Mg, Ca, Sr), *J. Phys. Chem. Solids*, 2004, **187**, 111859.

28 P. Blaha, K. Schwarz, G. K. H. Madsen, D. Kvasnicka and J. Luitz, *WIEN2k; an Augmented Plane Wave Plus Local Orbital Program for Calculating Crystal Properties*, Vienna University of Technology, Austria, 2001.

29 Z. Wu and R. E. Cohen, More accurate generalized gradient approximation for solids, *Phys. Rev. B: Condens. Matter Mater. Phys.*, 2006, **73**, 235116.

30 J. P. Perdew, K. Burke and M. Ernzerhof, Generalized gradient approximation made simple, *Phys. Rev. Lett.*, 1996, **77**, 3865.

31 E. Engel and S. H. Vosko, Exact exchange-only potentials and the virial relation as microscopic criteria for generalized gradient approximations, *Phys. Rev. B: Condens. Matter*, 1993, **47**, 13164.

32 Z. Ali, I. Ahmed, I. Khan and B. Amin, Electronic structure of cubic perovskite SnTaO3, *Intermetallics*, 2012, **31**, 287.

33 G. Murtaza, I. Ahmed, B. Amin and M. Zahid, Investigation of structural and optoelectronic properties of BaThO3, *Opt. Mater.*, 2011, **33**, 553.

34 H. Jiang, Band gaps from the Tran-Blaha modified Becke-Johnson approach: A systematic investigation, *J. Chem. Phys.*, 2013, **138**, 134115.

35 J. A. Camargo-Martinez and R. Baquero, Performance of the modified Becke-Johnson potential for semiconductors, *Phys. Rev. B: Condens. Matter Mater. Phys.*, 2012, **86**, 195106.

36 R. A. Jishi, O. B. Ta and A. A. Sharif, Modeling of lead halide perovskites for photovoltaic applications, *J. Phys. Chem. C*, 2014, **118**, 28344–28349.

37 R. A. Jishi, Modified Becke-Johnson exchange potential: improved modelling of lead halides for solar cell applications, *AIMS Mater. Sci.*, 2016, **3**, 149–159.

38 M. Z. ur Rehman, S. A. Abdelmohsen, E. A. Mahmoud, M. U. Saeed, M. Idress, M. Shafiq, B. Amin and Y. Saeed, First principles study of structural, electronic, elastic and optical properties of $Cs_2LiTlBr_6$ and $Cs_2NaTlBr_0$, *Mater. Sci. Semicond. Process.*, 2022, **151**, 106993.

39 Y. Saeed, B. Amin, H. Khalil, F. Rehman, H. Ali, M. I. Khan, A. Mahmood and M. Shafiq, $Cs_2NaGaBr_6$: a new lead-free and direct band gap halide double perovskite, *RSC Adv.*, 2020, **10**, 17444–17451.

40 U. Khan, M. U. Saeed, H. O. Elansary, I. M. Moussa and Y. Saeed, A DFT study of bandgap tuning in chloro-fluoro silicene, *RSC Adv.*, 2024, **14**, 4844–4852.

41 M. Usman Saeed, T. Usman, S. Pervaiz, Z. Ali, Y. Mohammed Alanazi, A. U. R. Bacha and Y. Saeed, DFT Analysis of Alkali Scandium Sulfides AScS 2 (A = K, Rb): Unveiling Structural, Electronic, and Optical Properties for Enhanced Photocatalysis", *ACS Appl. Opt. Mater.*, 2024, **2**, 1955–1964.

42 C. Y. Wang, S. R. Li, S. F. Wang, P. X. Zhao, R. S. Zhuo and B. Y. Yu, Effect of biaxial Pre-proof strain on monolayer MoS_2 and its vacancy defect system: a first-principles study, *J. Solid State Chem.*, 2023, **317**, 123711.

43 J. Liang, C. Wang, Y. Wang, Z. Xu, Z. Lu, Y. Ma, H. Zhu, Y. Hu, C. Xiao, X. Yi, G. Zhu, H. Lv, L. Ma, T. Chen, Z. Tie, Z. Jin and J. Liu, All-Inorganic Perovskite Solar Cells, *J. Am. Chem. Soc.*, 2017, **139**, 2852.

44 E. T. McClure, M. R. Ball, W. Windl and P. M. Woodward, Cs_2AgBiX_6 (X= Br, Cl): new visible light absorbing, lead-free halide perovskite semiconductors, *Chem. Mater.*, 2016, **28**, 1348.

45 J. Liang, C. Wang, Y. Wang, Z. Xu, Z. Lu, Y. Ma, H. Zhu, Y. Hu, C. Xiao, X. Yi, G. Zhu, H. Lv, L. Ma, T. Chen, Z. Tie, Z. Jin and J. Liu, All-inorganic perovskite solar cells, *J. Am. Chem. Soc.*, 2016, **138**, 15829–15832.

46 Z. Abbas, N. Jabeen, A. Hussain, F. Kabir, T. Alshahrani, H. H. Raza, S. Muhammad, S. Azam and I. Gorczyca, Effect of Nb, Ta and V replacements on electronic, optical and elastic properties of $NbCu_3Se_4$: a GGA+U study", *J. Solid State Chem.*, 2021, **301**, 122338.

47 P. Mondal, N. A. Shahed, S. Khanom, M. K. Hossain and F. Ahmed, Effect of oxygen defects in tuning the half-metallic and optical nature of Sr2CoXO6 (X = Mo and W): a first-principles study, *Mater. Chem. Phys.*, 2022, **277**, 125429.

48 L. D. Whalley, J. M. Frost, Y. K. Jung and A. Walsh, Perspective: Theory and simulation of hybrid halide perovskites, *J. Chem. Phys.*, 2017, **146**, 220901.
49 D. Y. Hu, X. H. Zhao, T. Y. Tang, L. Li, L. K. Gao and Y. L. Tang, First-principles calculations to investigate structural, elastic, electronic and optical properties of lead-free perovskite derivatives Cs2SeX6 (X = Cl, Br, I), *Opt. Mater.*, 2021, **119**, 111316.
50 L. Y. Gong, P. Zhang, Q. Chen, Z. H. Lou, J. Xu and F. Gao, First principles study of structure and property of Nb5+ doped SrTiO3, *Acta Phys. Sin.*, 2021, **70**, 227101.
51 E. Oyeniyi, Electronic and optical properties of Mg3XN (X = P, As, Sb, Bi) antiperovskites: the GW/BSE approach", *Solid State Commun.*, 2022, **355**, 114927.
52 W. F. Goh and W. E. Pickett, Topological and thermoelectric properties of double antiperovskite pnictides, *J. Phys.: Condens. Matter*, 2020, **32**, 345502.
53 C. Y. Wang, S. R. Li, S. F. Wang, P. X. Zhao, R. S. Zhuo and B. Y. Yu, Effect of biaxial[110] strain on monolayer MoS2 and its vacancy defect system: a first-principles study", *J. Solid State Chem.*, 2023, **317**, 123711.
54 Z. Abbas, N. Jabeen, A. Hussain, F. Kabir, T. Alshahrani, H. H. Raza, S. Muhammad, S. Azam and I. Gorczyca, Effect of Nb, Ta and V replacements on electronic, optical and elastic properties of $NbCu_3Se_4$: a GGA+U study", *J. Solid State Chem.*, 2021, **301**, 122338.
55 P. Mondal, N. A. Shahed, S. Khanom, M. K. Hossain and F. Ahmed, Effect of oxygen defects in tuning the half-metallic and optical nature of Sr2CoXO6 (X = Mo and W): a first−principles study, *Mater. Chem. Phys.*, 2022, **277**, 125429.
56 S. Berri, Theoretical analysis of the structural, electronic and optical properties of tetragonal Sr2GaSbO6, *Chin. J. Phys.*, 2017, **55**, 2476–2483.
57 K. Maeda and K. Domen, Photocatalytic water splitting: recent progress and future challenges, *J. Phys. Chem. Lett.*, 2010, **1**, 2655–2661.
58 R. M. Navarro Yerga, M. C. Alvarez Galvan, F. Del Valle, J. A. Villoria de la Mano and J. L. Fierro, Water splitting on semiconductor catalysts under visible-light irradiation, *Chem. Sustain. Ener. Mater.*, 2009, **2**, 471–485.
59 F. E. Osterloh, Inorganic materials as catalysts for photochemical splitting of water, *Chem. Mater.*, 2008, **20**, 35–54.
60 X. Hu, G. Li and J. C. Yu, Design, fabrication and modification of nanostructured semiconductor materials for environmental and energy applications, *Langmuir*, 2010, **26**, 3031–3039.
61 A. Kudo, Photocatalysis and solar hydrogen production, *Pure Appl. Chem.*, 2007, **79**, 1917–1927.
62 J. Liu, X. Fu, S. Chen and Y. Zhu, Electronic structure and optical properties of Ag_3PO_4 photocatalyst calculated by hybrid density functional method, *Appl. Phys. Lett.*, 2011, **99**, 191903.
63 M. Saeed, I. U. Haq, A. S. Saleemi, S. U. Rehman, B. U. Haq, A. R. Chaudhry and I. Khan, First-principles prediction of the ground-state crystal structure of double-perovskite halides Cs_2AgCrX_6 (X = Cl, Br, and I), *J. Phys. Chem. Solids*, 2022, **160**, 110302.
64 J. Li and H. Chen, First-principles investigation of the mechanical and thermodynamic properties of the antiperovskite centrosymmetric platinum-based superconductors APt3P (A = Ca, Sr, La and Ce), *Phys. B*, 2020, **577**, 411791.
65 M. Y. Rudysh, M. Piasecki, G. L. Myronchuk, P. A. Shchepanskyi, V. Y. Stadnyk, O. R. Onufriv and M. G. Brika, $AgGaTe_2$ The thermoelectric and solar cell material: structure, electronic, optical, elastic and vibrational features, *Infrared Phys. Technol.*, 2020, **111**, 103476.
66 B. T. Wang, W. X. Zhang and W. D. Li, Mechanics, Lattice dynamics, and chemical bonding in ZrB_2 and ZrB_2 from first-principles calculations, *Sci. Adv. Mater.*, 2013, **5**, 1916–1921.
67 X. H. Zhao, Y. L. Tang, T. Y. Tang, X. F. Diao, L. K. Gao, Q. Xie, B. Shi, L. Yuan and L. M. Lu, Study on mechanical, electronic and optical properties of Pb-free double halide perovskites In2TiX6 (X = Cl, Br, I) for solar cells based on first-principles, *Mater. Today Commun.*, 2021, **26**, 102180.
68 L. K. Gao, X. H. Zhao, X. F. Diao, T. Y. Tang and Y. L. Tang, First-principles study of photoelectric properties of CsSnBr3 under hydrostatic pressure, *Acta Phys. Sin.*, 2021, **70**, 158801.
69 J. Li and H. Chen, First-principles investigation of the mechanical and thermodynamic properties of the antiperovskite centrosymmetric platinum-based superconductors APt3P (A = Ca, Sr, La and Ce), *Phys. B*, 2020, **577**, 411791.
70 R. Gaillac, P. Pullumbi and F. X. Coudert, ELATE: An open-source online application for analysis and visualization of elastic tensors, *J. Phys.: Condens. Matter*, 2016, **28**, 275201.
71 S. I. Ranganathan and M. Ostoja-Starzewski, Universal elastic anisotropy index, *Phys. Rev. Lett.*, 2008, **101**, 055504.
72 S. F. Pugh, XCII. Relations between the elastic moduli and the plastic properties of polycrystalline pure metals, *Philos. Mag., Ser. 5*, 1954, **45**, 823.
73 M. Y. Sofi and D. C. Gupta, Scrutinized the inherent spin half-metallicity and thermoelectric response of ff-electron-based RbMO3 (M = Np, Pu) perovskites: A computational assessment, *Sci. Rep.*, 2022, **12**, 19476.
74 A. Togo, L. Chaput, T. Tadano and I. Tanaka, Implementation strategies in phonopy and phono3py, *J. Phys.: Condens. Matter*, 2023, **35**, 353001.
75 A. Togo, First-principles Phonon Calculations with Phonopy and Phono3py, *J. Phys. Soc. Jpn.*, 2023, **92**, 012001.
76 Q. Mahmood, M. Yaseen, M. Hassan, M. S. Rashid, I. Tlili and A. Laref, The first-principle study of mechanical, optoelectronic and thermoelectric properties of CsGeBr3 and CsSnBr3 perovskites, *Mater. Res. Express*, 2019, **6**, 045901.
77 S. Kuma and M. M. Woldemariam, Structural, electronic, lattice dynamic, and elastic properties of $SnTiO_3$ and $PbTiO_3$ using density functional theory, *Adv. Condens. Matter Phys.*, 2019, **2019**, 1–12.
78 Z. Sun, S. Li, R. Ahuja and J. M. Schneider, Calculated elastic properties of M_2AlC (M = Ti, V, Cr, Nb and Ta), *Solid State Commun.*, 2004, **129**, 589–592.